3D Research manuscript No.
(will be inserted by the editor)

Construction of extended 3D field of views of the internal bladder wall surface: a proof of concept

Achraf Ben-Hamadou · Christian Daul · Charles Soussen

arXiv:1607.04773v1 [cs.CV] 16 Jul 2016

Received: 29 February 2016 / Revised: 25 May 2016 / Accepted: 30 May 2016

Abstract 3D extended field of views (FOVs) of the internal bladder wall facilitate lesion diagnosis, patient follow-up and treatment traceability. In this paper, we propose a 3D image mosaicing algorithm guided by 2D cystoscopic video-image registration for obtaining textured FOV mosaics. In this feasibility study, the registration makes use of data from a 3D cystoscope prototype providing, in addition to each small FOV image, some 3D points located on the surface. This proof of concept shows that textured surfaces can be constructed with minimally modified cystoscopes. The potential of the method is demonstrated on numerical and real phantoms reproducing various surface shapes. Pig and human bladder textures are superimposed on phantoms with known shape and dimensions. These data allow for quantitative assessment of the 3D mosaicing algorithm based on the registration of images simulating bladder textures.

Keywords Cystoscopy · 3D mosaicing · 3D endoscope prototype · textured surface registration · mutual information

1 Introduction

In the United States, bladder cancer is the fourth and ninth most widespread cancer among males and females, respectively, whereas in Europe, approximately 50,000 people die from this disease each year [2]. Due to the high recurrence rate of 50%, lifetime monitoring of patients is required after surgical removal of cancer tumors [18]. During a cystoscopy, a flexible or rigid endoscope is inserted into the bladder through the urethra, and a video of the epithelium is visualized on a screen. The clinician (urologist or surgeon) scans the epithelium by maintaining the distal tip of the cystoscope close to the internal organ wall. The resulting highly resolved videos yield accurate visualization of the wall through small field of view (FOV) images. However, neither complete regions of interest (multifocal lesions, scares, etc.) nor anatomical landmarks (urethra, ureters, air bubbles) are visible in these images. Therefore, lesion diagnosis and follow-up may be difficult and time-consuming. Extended FOV mosaics can be obtained by superimposing the regions which can be jointly observed in small FOV images. Not only do they facilitate lesion diagnosis and follow-up, but they are also useful for data archiving (videos are highly redundant data) and medical traceability (videos are not easy to interpret by a clinician having not performed the acquisition).

1.1 Bladder image mosaicing

Bi-dimensional (2D) bladder image mosaicing algorithms were proposed for the standard white-light modality [12,22] and for the fluorescence modality [6]. A complete mosaicing algorithm consists of *(i)* the registration of consecutive images of the video sequence [17], *(ii)* the correction of image misalignment in the mosaic leading to bladder texture discontinuities [30], and *(iii)* the contrast, intensity and/or color correction to handle image blurring, shading effects and/or instru-

A. Ben-Hamadou · C. Daul (✉) · C. Soussen
Université de Lorraine and CNRS. CRAN, 2 avenue de la Forêt de Haye, F-54518 Vandœuvre-lès-Nancy, France
Tel.: +33 3 83 59 57 15
Fax: +33 3 83 59 56 44
E-mail: christian.daul@univ-lorraine.fr
Current affiliation: A. Ben-Hamadou
Valeo, Driving Assistance Research, 34 rue St-André Z.I. des Vignes, 93012 Bobigny, France

ment viewpoint changes [8,29]. In [30], it was shown that mosaics covering large bladder surfaces (*e.g.*, half of the organ) can be computed. Although such 2D mosaics (see Fig. 1) facilitate lesion diagnosis and follow-up, these representations can be improved. Indeed, only the first image of the mosaic has the original image resolution, the resolution of the other images depending on the instrument trajectory and orientation. Moreover, these images are strongly distorted during their placement into the 2D map due to perspective changes of the endoscope. Both image distortion and changes of resolution lead to mosaics with spatially-varying visual quality. At last, urologists or surgeons represent themselves the bladder in the three-dimensional (3D) space. Mosaics in 3D (*i.e.*, bladder wall surfaces with superimposed 2D image textures) not only match this mental 3D representation, but allow for a bladder texture representation without any image distortion and with preserved resolution. Moreover, virtual navigation inside the reconstructed organ part is possible after clinical examinations using 3D mosaics. The interest of 2D and 3D endoscopic image mosaicing in various medical fields is discussed in the overview paper [11].

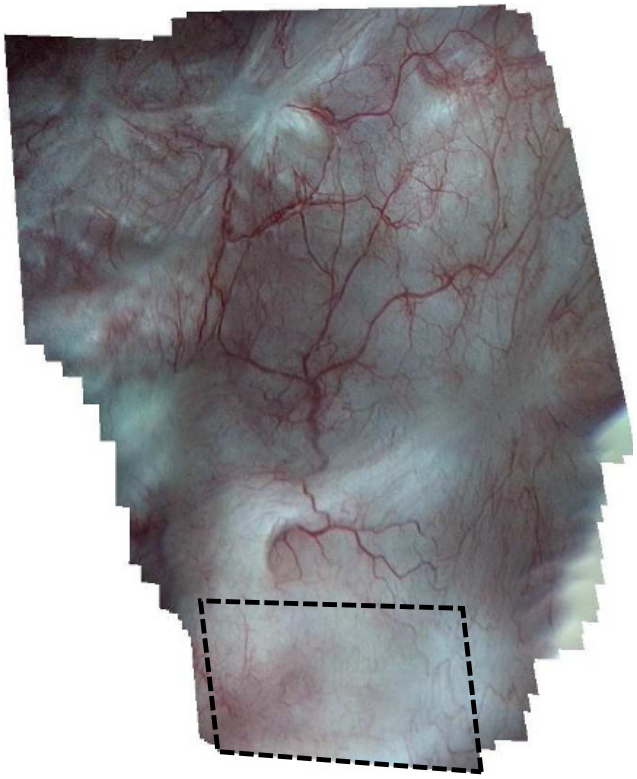

Fig. 1 Bladder mosaic (clinical data) obtained with the registration algorithm [30] and using the algorithm [29] for correction of illumination discontinuities. The first image of the sequence is at the top right. From this image position, the endoscope first moves downwards in the bright regions (dashed bounding box) with weak textures. Then, its trajectory goes up towards the last image at the top left. Strong perspective and scale changes arise between the first and last images.

1.2 Previous work in 3D endoscopic data mosaicing

In various fields of medical endoscopy, 3D mosaics are built following three kinds of approaches.

In the first approach, analytically known surface shapes (representing organs) are used both to limit the 2D registration errors and visualize textured surfaces. In [7], bladder hemispheres were approximated by hemicubes whose five sides represent quasi planar bladder regions. A video sequence was then partitioned into image groups, each group corresponding to some hemicube side. The five reconstructed 2D sub-mosaics were then projected onto the hemisphere to obtain a 3D bladder representation. As for the inner esophagus wall [14], the organ was approximated by tubular shapes. The registration method aligns endoscopic images using jointly the image colors and a mosaicing surface of known geometry to reduce distortions. This algorithm provides both the endoscope trajectory and a 2D mosaic that can be projected onto the inner cylinder surfaces. Such approach based on 3D prior models is well-suited to the esophagus which can indeed be modelled by tubes, but is less appropriate for 3D bladder mosaicing. Indeed, the bladder shape is hardly predictable, notably since it is deformed by neighboring organs putting pressure on it. Moreover, grouping images with respect to hemicube sides is time-consuming and difficult.

In the second approach, no 3D prior information is imposed, *i.e.*, only video-images are taken into account. Different passive vision methods were proposed based on shape from shading (SfS [31], bone surface reconstruction), structure from motion (SfM [28], cystoscopy), shape from motion associated to SfS ([19], colon surface reconstruction), SfM-factorization based on surgical instrument tracking ([32], surgery) or simultaneous localization and mapping methods (SLAM [23], laparoscopy for minimal invasive surgery). The lack of intensity variation in standard bladder images impedes SfS. However, SfM or SLAM methods may be appropriate in urology. In their 3D bladder mosaicing feasibility study [28], Soper *et al* replaced the endoscope standardly used in urology by an ultrathin fiber. The fiber was translated and rotated in such a way that a complete bladder scan is performed. The acquired image sequence was first used to find point correspondences in image pairs using homologous feature points. Then, the 3D surface was constructed by displacing a set of points initially located on a sphere. Specifically, a bundle adjustment method was used to iteratively determine both fiber tip trajectory and pig bladder

phantom surface. The main limitation of this approach for standard cystoscopy is that salient texture points must be extracted from the video-images. In large human bladder regions, textures may be missing or very weakly contrasted for both healthy (see the bottom of the mosaic in Fig. 1) and damaged tissues, *e.g.*, due to scares. In such images, SfM or SLAM techniques based on SIFT or SURF approaches for extracting and matching textures thus suffer from a lack of robustness (see [5,17] for a detailed discussion on feature based techniques in cystoscopy). Feature point extraction and matching techniques is also difficult because of illumination changes occurring between images, which are due to strong perspective changes and/or the vignetting effect of endoscopes. Another major limitation of feature-based methods is blur, which is commonly encountered in standard cystoscopy images.

A less investigated approach in 3D endoscopy is based on active vision, where surface points are reconstructed in the small FOV of modified endoscopes. In [15], a two-channel endoscope was used to reconstruct the inner surface of the mouth. The first channel projects a structured-light pattern whereas the second acquires video-images. Classical triangulation methods were used to reconstruct 3D points. Tests on phantoms have shown that submillimetre point reconstruction accuracy can be reached with a small baseline of 2 mm. Another acquisition setup [25] consists of a classical CCD-camera and a time of flight (ToF) camera providing a depth map of the FOV. A calibration procedure provides for each pixel both a color and a 3D position with millimetre accuracy. In [25], a two-channel endoscope (laparoscope) was used to reconstruct points in a pig stomach. It is noticeable that such camera pair can be used as well for single channel endoscopes such as cystoscopes. Indeed, a ToF camera uses infrared signals that do not interfere with the visible light of a color camera. Shevchenko *et al* proposed a structured-light approach for obtaining extended 3D bladder surfaces [27]. The prototype in [27] consists of an external navigation system (which localizes the endoscope position in the examination room) coupled with an endoscopic system projecting a grid of points on the inspected surface. The 3D surface was built by computing a 2D mosaic from the CCD camera images, and exploiting the information provided by the external system. Knowing the endoscope position and the 2D image correspondence, the 2D mosaic has to be projected onto the reconstructed surface. It is noticeable that in [1], the authors also proposed a navigation system based method to document the position of a lesion into the bladder during a first cystoscopy. The aim was not 3D image mosaicing, but rather to facilitate follow-up by performing fast localization of lesions in upcoming cystoscopies. In the conference paper [9], we proposed the first active vision based approach for 3D bladder mosaicing. Based on a similar structured light principle as that described later in [27], the proposed solution did however not require any external navigation system for endoscope localization. The 3D surface construction algorithm was based on 2D image registration and on the reconstruction of 3D points in the coordinate system of the endoscope camera. However, the proof of concept of 3D cystoscopy was only partly established in [9]. The algorithm was not tested using data (2D images and 3D points) acquired with the structured light principle embedded in a cystoscope. The related data were acquired for a large baseline (distance between the focal lengths of the camera and the light projector) of about 150 mm. This approach was not yet evaluated in the less favorable case of small baselines of 2 to 3 mm, like in cystoscopy. Furthermore, the image processing algorithm in [9] needed to be improved. It was based on a registration step, where the squared difference between image grey-levels was minimized. This approach is not robust when textures are weakly contrasted or with high inter- and intra-patient variability. Such similarity measure is also not appropriate to the illumination changes occurring in cystoscopic data.

1.3 Objectives

The medical objective of the scanning fiber endoscope described in [28] was to design a procedure where bladder walls can be fully acquired by nurses or ancillary care providers. This allows for sparing the time of urologists who can post-operatively review the bladder data. Such procedure is currently not standard but may be complementary to the usual examination with flexible or rigid cystoscopes. In the present paper, we aim to establish the proof of concept of bladder mosaicing using 3D cystoscopes based on active vision, which is a promising approach as shown in [27]. In [28], the distal tip of the fiber follows a spiral shaped trajectory and the distance from the optical center to the bladder wall is in average larger than the acquisition distance with cystoscopes. This allows for the use of the SfM approach. This is no longer true with cystoscopy, since depth disparity is often not guaranteed. Moreover, the lack of textures (as in the bounding box of Fig. 1) also complicates SfM approaches, which require robust and accurate homologous point correspondence between images. In the present 3D bladder mosaicing feasibility study, an active vision solution is chosen. As compared to [27], our goal is to show that a 3D mosaicing algorithm guided by image registration is useful for retriev-

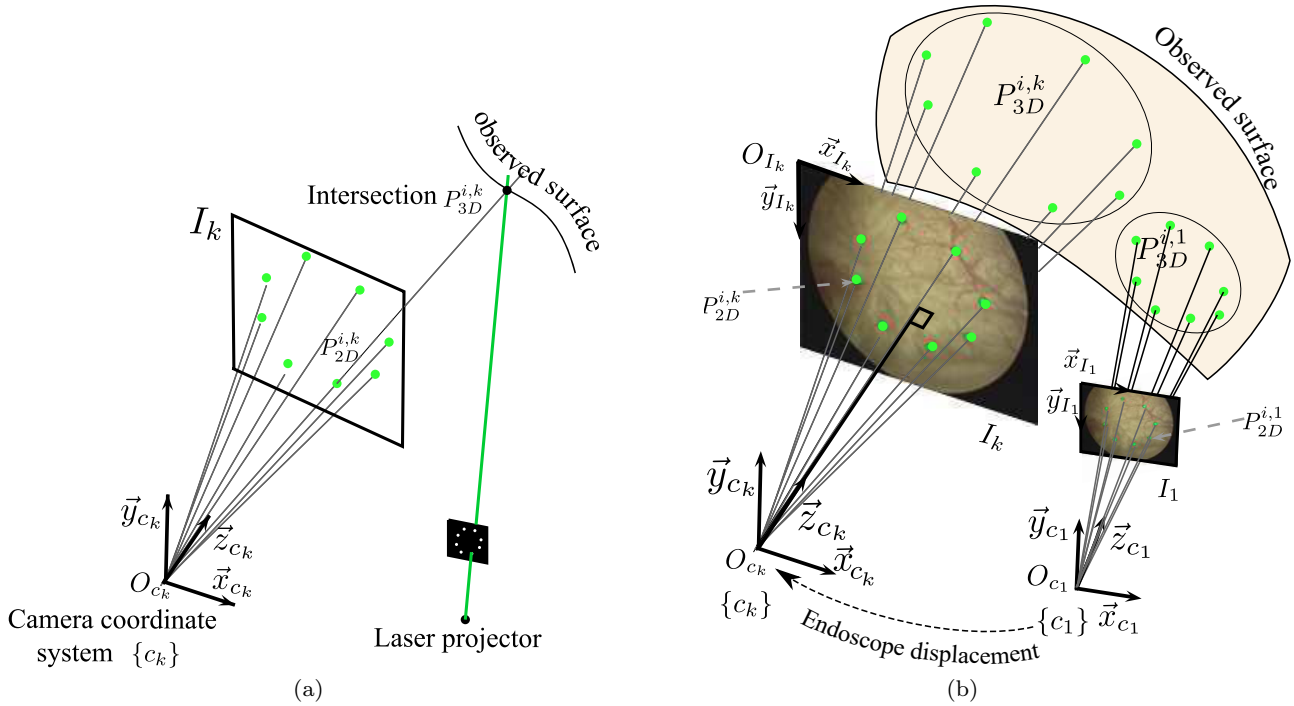

Fig. 2 Acquisition principle (a) and available data (b) for 3D mosaicing. The acquisition principle is implemented using the prototype of Section 4. (a) The i-th "projector ray" is shown in green. The corresponding "camera ray" is the black line originating from point $P_{3D}^{i,k}$ of the surface (intersection of the projector and camera rays) and passing through the optical center O_{c_k} of the camera. $P_{2D}^{i,k}$ is the intersection of the camera ray with the plane supporting the acquired image I_k. (b) The available data are represented for the first and k-th acquisitions. The camera coordinate system $\{c_k\}$ reads $(O_{c_k}, \overrightarrow{x_{c_k}}, \overrightarrow{y_{c_k}}, \overrightarrow{z_{c_k}})$ and moves together with the prototype. The black line in bold represents the camera focal distance f, calibrated as described in [10].

ing the endoscope displacement between two acquisitions without using external navigation systems. From the instrumentation viewpoint, we show that 3D bladder mosaicing is feasible by simply modifying standard cystoscopes. Although the proposed prototype cannot currently be used in clinical situation, our 3D point reconstruction approach can be implemented on cystoscopes. Furthermore, it was shown that 3D point reconstruction is accurate enough, even for small baselines of point triangulation [10,15].

From the image processing viewpoint, we propose a 3D image mosaicing algorithm for which no assumption has to be made regarding the endoscope trajectory. The unknown endoscope displacement between consecutive image acquisitions is a general combination of a 3D rotation and a 3D translation. Although real-time mosaicing can be of interest, the computation time is not the most critical point in urology. As argued in [22, 30], a mosaicing time of some tens of minutes is acceptable for a second (finer) diagnosis carried out to confirm or modify the first diagnosis during the real-time visualization of the small FOV video-images. Real-time is neither a critical factor for lesion follow-up because the lesion evolution assessment is performed with data from a cystoscopy scheduled some weeks or months after the cystoscopy in progress.

The paper is organized as follows. Section 2 introduces the data acquisition principle (for readability reasons, the description of the prototype implementing this measurement principle is deferred to Section 4). Section 3 details the 3D mosaicing algorithm. In Section 4, the algorithm is tested on phantoms with various shapes allowing for a validation of the algorithm with data acquired by the proposed 3D cystoscope prototype. In Section 5, simulated data allow for qualitative evaluation on more realistic bladder data, in terms of both 3D surface shape and bladder texture. Section 6 exhibits the 3D registration errors obtained for both synthetic data and data related to the prototype. Concluding remarks and perspectives are given in Section 7.

2 Acquisition principle and available data

The principle of our laser based active vision system is sketched in Fig. 2(a). The prototype is equipped with a color camera and a structured laser light projector. The basic idea is to project laser rays, such as the green line of Fig. 2(a), onto the bladder epithelial surface.

Then, each projector ray is being reflected by the surface. This generates a so-called "camera ray" (the black line of Fig. 2(a)) passing through the green laser dots visible in image I_k. In Fig. 2(a), the quadrangle with black background corresponds to diffractive optics, *i.e.*, holographic binary phase lens, designed to project eight laser rays. The latter are located on a cone originating from the projector optical center. Each projector ray passes through one of the eight white dots of the diffractive optics. For readability matters, only one ray is shown in Fig. 2(a).

The calibration procedure in [10] is used to compute the intrinsic and extrinsic camera and projector parameters. The parameters of the projector ray equations are computed in the camera coordinate system $(O_{c_k}, \overrightarrow{x_{c_k}}, \overrightarrow{y_{c_k}}, \overrightarrow{z_{c_k}})$, referred to as $\{c_k\}$, with O_{c_k} the optical center of the camera. Because the projector and camera are rigidly fixed together, the equations of the projector rays in $\{c_k\}$ do not depend on k. The equations of the camera rays (passing all through O_{c_k}) are also computed in $\{c_k\}$ given the location $P_{2D}^{i,k}$ of the green dots in image I_k (i stands for the index of the green dots). The green dots can be easy segmented since the hue of the bladder is always reddish or orange, see the real images of Figs. 1 and 2(b). The i-th laser point on the bladder surface ($P_{3D}^{i,k}$) is the intersection of the projector ray with its corresponding camera ray.

The data available for 3D mosaicing are related to a video-sequence with K frames. Each acquisition $k \in \{1, \ldots, K\}$ corresponds to a cystoscope viewpoint and yields: *(i)* an image I_k; *(ii)* eight laser dots $P_{2D}^{i,k} = (x_{2D}^{i,k}, y_{2D}^{i,k})^T$ given in the coordinate system $(O_{I_k}, \overrightarrow{x_{I_k}}, \overrightarrow{y_{I_k}})$ of the plane supporting I_k; *(iii)* eight laser points $P_{3D}^{i,k} = (x_{3D}^{i,k}, y_{3D}^{i,k}, z_{3D}^{i,k})^T$ given in the camera coordinate system $\{c_k\}$ (see Fig. 2(b)). The barrel distortions in images I_k are corrected using the known intrinsic camera parameters [10]. The laser rays ($i \in \{1, \ldots, M\}$ with $M = 8$) are projected in the periphery of the circular FOV of the images to minimize the loss of bladder texture and to allow for diagnosis. Although only eight $P_{3D}^{i,k}$ points are available per viewpoint, the video acquisition leads to a large number of points overall due to the high acquisition speed (25 images/s) and the slow endoscope displacements (some mm/s).

The algorithm proposed in Section 3 aims at placing all points $P_{3D}^{i,k}$ in a common coordinate system, and then computing a polygonal mesh representing the smooth bladder surface, without corners nor sharp edges. The textures of images I_k will finally be projected onto the polygonal mesh.

3 Construction of three-dimensional textured surfaces

The proposed 3D mosaicing method takes as inputs a set of distortion-corrected images I_k and a set of $M = 8$ points per viewpoint k. Each $P_{3D}^{i,k}$ point is given in the local (moving) coordinate system $\{c_k\}$ of the camera. Moreover, their 2D projections $P_{2D}^{i,k}$ in the k-th image of the video-sequence ($i = 1, \ldots, M$) are known as well. The algorithm for reconstructing the $P_{3D}^{i,k}$ points from the knowledge of their projections $P_{2D}^{i,k}$ can be found in [10].

The mosaicing algorithm requires some geometric prerequisites, which are presented now.

3.1 Geometrical considerations

The first geometrical transformation involves the intrinsic camera parameters linking the 3D camera coordinate system $\{c_k\}$ to the 2D image plane coordinate system $(O_{I_k}, \overrightarrow{x_{I_k}}, \overrightarrow{y_{I_k}})$. In (1), the perspective projection matrix $\mathbf{K}$ is fully defined from the knowledge of the projection (u, v) of the camera optical center in image I_k, the focal length f, and the CCD-sensor size l_x and l_y along the $\overrightarrow{x_{I_k}}$ and $\overrightarrow{y_{I_k}}$ axes (see Fig. 2(b)):

$$\begin{bmatrix} P_{2D}^{i,k} \\ 1 \end{bmatrix} = \frac{1}{z_{3D}^{i,k}} \mathbf{K}\, P_{3D}^{i,k} \text{ with } \mathbf{K} = \begin{bmatrix} f/l_x & 0 & u \\ 0 & f/l_y & v \\ 0 & 0 & 1 \end{bmatrix}. \quad (1)$$

The second transformation is a 3D rigid transformation linking consecutive camera viewpoints. It is parameterized by a 3×4 matrix $\mathbf{T}_{3D}^{k-1,k}$. $\mathbf{T}_{3D}^{k-1,k}$ is composed of a 3×3 rotation matrix $\mathbf{R}^{k-1,k}$ and a 3×1 translation vector $D^{k-1,k}$:

$$\hat{P}_{3D}^{i,k-1} = \mathbf{T}_{3D}^{k-1,k} \begin{bmatrix} P_{3D}^{i,k} \\ 1 \end{bmatrix}, \quad (2)$$

with

$$\mathbf{T}_{3D}^{k-1,k} = \left[\mathbf{R}^{k-1,k} \middle| D^{k-1,k} \right]. \quad (3)$$

The coefficients of the rotation matrix are defined from the well-known Euler angles, denoted by $\theta_1^{k-1,k}$, $\theta_2^{k-1,k}$ and $\theta_3^{k-1,k}$. The so-called "x-convention" is used for these angles: $\theta_1^{k-1,k} \in [0, 2\pi]$ is the angle around the $\overrightarrow{z_{c_k}}$-axis, $\theta_2^{k-1,k} \in [0, \pi]$ is around the new (rotated) $\overrightarrow{x_{c_k}}'$-axis, while $\theta_3^{k-1,k} \in [0, 2\pi]$ is around the rotated $\overrightarrow{z_{c_k}}''$-axis. Superscripts $'$ and $''$ respectively refer to the new location of axes $\overrightarrow{x_{c_k}}$ and $\overrightarrow{z_{c_k}}$ after the first and second rotations. The matrix $\mathbf{T}_{3D}^{k-1,k}$ displaces point $P_{3D}^{i,k}$ in $\{c_k\}$ to $\hat{P}_{3D}^{i,k-1} = (\hat{x}_{3D}^{i,k-1}, \hat{y}_{3D}^{i,k-1}, \hat{z}_{3D}^{i,k-1})^T$ in $\{c_{k-1}\}$.

It is worth noticing that $\hat{P}_{3D}^{i,k-1}$ are points brought within $\{c_{k-1}\}$ whereas $P_{3D}^{i,k-1}$ are "data points" reconstructed in $\{c_{k-1}\}$ using the calibration parameters and the segmented dots $P_{2D}^{i,k-1}$. Thus, $P_{3D}^{i,k-1}$ and $\hat{P}_{3D}^{i,k-1}$ represent different laser points.

The third relationship required by the proposed method is a homography linking two consecutive images I_k and I_{k-1}. This 2D relationship is established under several working assumptions. First, the distal tip of the cystoscope is usually close to the inner bladder epithelium. The FOV being very limited, the surfaces viewed in the images are usually small and are assumed to be planar. Second, the bladder is filled by an isotonic saline solution which rigidifies the bladder wall. The acquisition speed being high (25 image/s) and the endoscope displacement speed low (some mm/s), we assume that the common surface part viewed in images I_{k-1} and I_k does not warp itself between two consecutive acquisitions. Based on these working assumptions, the homography is well-suited to model the dependence between I_k and I_{k-1}. This choice was practically validated for numerous algorithms for 2D/2D registration of bladder images: feature-based methods in [7] (fluorescence modality) and [12,28] (white-light modality), the graph-cut method in [30] and two optical flow methods in [3,4]. The homography matrix is defined by:

$$\mathbf{T}_{2D}^{k-1,k} = \begin{bmatrix} \underbrace{\alpha^{k-1,k}\cos\varphi^{k-1,k}}_{a_{1,1}^{k-1,k}} & \underbrace{-s_x^{k-1,k}\sin\varphi^{k-1,k}}_{a_{1,2}^{k-1,k}} & \underbrace{t_{x,2D}^{k-1,k}}_{a_{1,3}^{k-1,k}} \\ \underbrace{s_y^{k-1,k}\sin\varphi^{k-1,k}}_{a_{2,1}^{k-1,k}} & \underbrace{\alpha^{k-1,k}\cos\varphi^{k-1,k}}_{a_{2,2}^{k-1,k}} & \underbrace{t_{y,2D}^{k-1,k}}_{a_{2,3}^{k-1,k}} \\ a_{3,1}^{k-1,k} & a_{3,2}^{k-1,k} & 1 \end{bmatrix} \tag{4}$$

where the parameters α, φ, (s_x, s_y) and $(t_{x,2D}, t_{y,2D})$ respectively denote the scale factor, in-plane rotation, shearing and 2D translation changes. In the following and for simplicity reasons, the matrix $\mathbf{T}_{2D}^{k-1,k}$ will be simply described by means of its coefficients $a_{r,s}^{k-1,k}$.

Image I_k is registered with I_{k-1} when $\mathbf{T}_{2D}^{k-1,k}$ superimposes homologous points P_{2D}^{k} and P_{2D}^{k-1} of both images, *i.e.*, when

$$\begin{bmatrix} P_{2D}^{k-1} \\ 1 \end{bmatrix} = \frac{1}{\beta^{k-1,k}}\ \mathbf{T}_{2D}^{k-1,k} \begin{bmatrix} P_{2D}^{k} \\ 1 \end{bmatrix}. \tag{5}$$

The normalizing factor $\beta^{k-1,k}$ deduces from the perspective parameters $a_{3,1}^{k-1,k}$ and $a_{3,2}^{k-1,k}$:

$$\beta^{k-1,k} = [a_{3,1}^{k-1,k}, a_{3,2}^{k-1,k}]^T P_{2D}^{k} + 1. \tag{6}$$

Let us stress that (5) is met for all homologous texture pixels of images I_k and I_{k-1} (P_{2D}^{k-1} and P_{2D}^{k}), but not for the laser points $P_{2D}^{i,k}$ and $P_{2D}^{i,k-1}$. Indeed, $P_{2D}^{i,k}$ and $P_{2D}^{i,k-1}$ are not homologous points because the active vision system is moving from viewpoint $k-1$ to viewpoint k. Nevertheless, (5) will be exploited to estimate the parameters of a candidate homography $\mathbf{T}_{2D}^{k-1,k}$ corresponding to a candidate $\mathbf{T}_{3D}^{k-1,k}$ transformation. Moreover, the quality of image superimposition will be assessed based on (5), applied to all homologous texture pixels of I_{k-1} and I_k.

3.2 Consecutive viewpoint registration

3.2.1 Principle of the registration algorithm

Let us define the displaced projected laser points $\hat{P}_{2D}^{i,k-1}$ as the 2D projections of the laser points $P_{3D}^{i,k}$, displaced from $\{c_k\}$ to $\{c_{k-1}\}$. Combining (1) and (2) yields:

$$\begin{bmatrix} \hat{P}_{2D}^{i,k-1} \\ 1 \end{bmatrix} = \frac{1}{\hat{z}_{3D}^{i,k-1}}\ \mathbf{K}\mathbf{T}_{3D}^{k-1,k} \begin{bmatrix} P_{3D}^{i,k} \\ 1 \end{bmatrix}. \tag{7}$$

Now, consider an ideal (and searched) $\mathbf{T}_{3D}^{k-1,k}$ transformation, whose related homography $\mathbf{T}_{2D}^{k-1,k}$ superimposes the pixels of I_k and their homologous pixels in I_{k-1}. Such $\mathbf{T}_{2D}^{k-1,k}$ transformation not only superimposes homologous texture pixels, but also relates each laser point $P_{2D}^{i,k}$ to its displaced instance $\hat{P}_{2D}^{i,k-1}$:

$$\begin{bmatrix} \hat{P}_{2D}^{i,k-1} \\ 1 \end{bmatrix} = \frac{1}{\beta_i^{k-1,k}}\ \mathbf{T}_{2D}^{k-1,k} \begin{bmatrix} P_{2D}^{i,k} \\ 1 \end{bmatrix}, \tag{8}$$

where the factor $\beta^{k-1,k}$ appearing in (5) has been replaced by $\beta_i^{k-1,k}$ to stress the dependence upon i. Combining (7) and (8) yields:

$$\frac{1}{\beta_i^{k-1,k}}\ \mathbf{T}_{2D}^{k-1,k} \begin{bmatrix} P_{2D}^{i,k} \\ 1 \end{bmatrix} = \frac{1}{\hat{z}_{3D}^{i,k-1}}\ \mathbf{K}\ \mathbf{T}_{3D}^{k-1,k} \begin{bmatrix} P_{3D}^{i,k} \\ 1 \end{bmatrix} \tag{9}$$

which involves the 2D and 3D laser points related to viewpoint k only.

For a given candidate $\mathbf{T}_{3D}^{k-1,k}$, $\hat{z}_{3D}^{i,k-1}$ is known from the last equation of (7) and the knowledge of $P_{3D}^{i,k}$. Similarly, $\beta_i^{k-1,k}$ can be deduced from $\mathbf{T}_{2D}^{k-1,k}$ using (6). Therefore, $\mathbf{T}_{3D}^{k-1,k}$ and $\mathbf{T}_{2D}^{k-1,k}$ are the only unknowns in (9). As we will see, $\mathbf{T}_{2D}^{k-1,k}$ can actually be deduced from $\mathbf{T}_{3D}^{k-1,k}$ and the knowledge of the laser points.

The proposed registration scheme is designed in such a way that some similarity measure (to be detailed) between both images I_k and I_{k-1} is maximized with respect to the $\mathbf{T}_{3D}^{k-1,k}$ parameters under the constraint formulated in (9). Each iteration of the optimization algorithm includes four steps related to the update and evaluation of the candidate $\mathbf{T}_{3D}^{k-1,k}$:

1. Update the rigid transformation $\mathbf{T}_{3D}^{k-1,k}$.
2. Compute matrix $\mathbf{T}_{2D}^{k-1,k}$ induced by $\mathbf{T}_{3D}^{k-1,k}$ using (9) and the location of the M laser points $(P_{3D}^{i,k}, P_{2D}^{i,k})$.
3. Superimpose I_{k-1} with $\mathbf{T}_{2D}^{k-1,k}(I_k)$, which denotes the transformation of image I_k using the computed homography $\mathbf{T}_{2D}^{k-1,k}$; see (5).
4. Evaluate the similarity measure between images I_{k-1} and $\mathbf{T}_{2D}^{k-1,k}(I_k)$ (the pixels of both images corresponding to laser dots are not taken into account).

This process terminates when the similarity measure between the registered images is maximal. This algorithm simultaneously provides the homography $\mathbf{T}_{2D}^{k-1,k}$ and the rigid transformation $\mathbf{T}_{3D}^{k-1,k}$ linking $\{c_k\}$ to $\{c_{k-1}\}$. Hereafter, we detail how $\mathbf{T}_{2D}^{k-1,k}$ is computed from $\mathbf{T}_{3D}^{k-1,k}$. Then, we define the similarity measure used for assessing the 2D image superimposition quality. Finally, an overview of the optimization algorithm is given (Algorithm 1).

3.2.2 Matrix relationship between $\mathbf{T}_{2D}^{k-1,k}$ and $\mathbf{T}_{3D}^{k-1,k}$

For a point correspondence $(P_{3D}^{i,k}, P_{2D}^{i,k})$, (9) is a system of three equations. Rearranging the first two equations and replacing $\beta_i^{k-1,k}$ and $\hat{z}_{3D}^{i,k-1}$ by their expressions, we obtain:

$$\begin{cases} \dfrac{\mathbf{T}_{2D,1\bullet}^{k-1,k}\begin{bmatrix} P_{2D}^{i,k} \\ 1 \end{bmatrix}}{\mathbf{T}_{2D,3\bullet}^{k-1,k}\begin{bmatrix} P_{2D}^{i,k} \\ 1 \end{bmatrix}} = \dfrac{\mathbf{K}_{1\bullet}\ \mathbf{T}_{3D}^{k-1,k}\begin{bmatrix} P_{3D}^{i,k} \\ 1 \end{bmatrix}}{\mathbf{T}_{3D,3\bullet}^{k-1,k}\begin{bmatrix} P_{3D}^{i,k} \\ 1 \end{bmatrix}} \\ \dfrac{\mathbf{T}_{2D,2\bullet}^{k-1,k}\begin{bmatrix} P_{2D}^{i,k} \\ 1 \end{bmatrix}}{\mathbf{T}_{2D,3\bullet}^{k-1,k}\begin{bmatrix} P_{2D}^{i,k} \\ 1 \end{bmatrix}} = \dfrac{\mathbf{K}_{2\bullet}\ \mathbf{T}_{3D}^{k-1,k}\begin{bmatrix} P_{3D}^{i,k} \\ 1 \end{bmatrix}}{\mathbf{T}_{3D,3\bullet}^{k-1,k}\begin{bmatrix} P_{3D}^{i,k} \\ 1 \end{bmatrix}} \end{cases} \tag{10}$$

where the subscripts $1\bullet$, $2\bullet$ and $3\bullet$ respectively index the first, second and third matrix rows and all column indices. Denoting by $c_{1,i}^{k-1,k}$ and $c_{2,i}^{k-1,k}$ the right-hand sides in (10), (10) rewrites:

$$\begin{cases} \mathbf{T}_{2D,1\bullet}^{k-1,k}\begin{bmatrix} P_{2D}^{i,k} \\ 1 \end{bmatrix} = c_{1,i}^{k-1,k}\ \mathbf{T}_{2D,3\bullet}^{k-1,k}\begin{bmatrix} P_{2D}^{i,k} \\ 1 \end{bmatrix} \\ \mathbf{T}_{2D,2\bullet}^{k-1,k}\begin{bmatrix} P_{2D}^{i,k} \\ 1 \end{bmatrix} = c_{2,i}^{k-1,k}\ \mathbf{T}_{2D,3\bullet}^{k-1,k}\begin{bmatrix} P_{2D}^{i,k} \\ 1 \end{bmatrix} \end{cases} \tag{11}$$

with

$$c_{1,i}^{k-1,k} = \left(\mathbf{K}_{1\bullet}\ \mathbf{T}_{3D}^{k-1,k}\begin{bmatrix} P_{3D}^{i,k} \\ 1 \end{bmatrix}\right) / \left(\mathbf{T}_{3D,3\bullet}^{k-1,k}\begin{bmatrix} P_{3D}^{i,k} \\ 1 \end{bmatrix}\right)$$
$$c_{2,i}^{k-1,k} = \left(\mathbf{K}_{2\bullet}\ \mathbf{T}_{3D}^{k-1,k}\begin{bmatrix} P_{3D}^{i,k} \\ 1 \end{bmatrix}\right) / \left(\mathbf{T}_{3D,3\bullet}^{k-1,k}\begin{bmatrix} P_{3D}^{i,k} \\ 1 \end{bmatrix}\right)$$

Replacing the points $P_{3D}^{i,k}$ and $P_{2D}^{i,k}$ by their coordinates, (11) yields a linear system of two equations involving the coefficients $a_{r,s}^{k-1,k}$ in (4):

$$\begin{cases} x_{2D}^{i,k}a_{1,1}^{k-1,k} + y_{2D}^{i,k}a_{1,2}^{k-1,k} + a_{1,3}^{k-1,k} - \dots \\ \quad c_{1,i}^{k-1,k}x_{2D}^{i,k}a_{3,1}^{k-1,k} - c_{1,i}^{k-1,k}y_{2D}^{i,k}a_{3,2}^{k-1,k} = c_{1,i}^{k-1,k} \\ x_{2D}^{i,k}a_{2,1}^{k-1,k} + y_{2D}^{i,k}a_{2,2}^{k-1,k} + a_{2,3}^{k-1,k} - \dots \\ \quad c_{2,i}^{k-1,k}x_{2D}^{i,k}a_{3,1}^{k-1,k} - c_{2,i}^{k-1,k}y_{2D}^{i,k}a_{3,2}^{k-1,k} = c_{2,i}^{k-1,k} \end{cases} \tag{12}$$

Both equations are valid for all laser points $P_{3D}^{i,k}$ of viewpoint k. This yields a linear system of $2M$ equations with eight unknown parameters $a_{r,s}^{k-1,k}$ related to transformation $\mathbf{T}_{2D}^{k-1,k}$: see (13). For our prototype, $M = 8$, so (13) is an over-determined system of 16 equations. Notice that when $M \geq 4$, the homography $\mathbf{T}_{2D}^{k-1,k}$ induced by $\mathbf{T}_{3D}^{k-1,k}$ is unique since there are $2M \geq 8$ equations in (13).

3.2.3 Similarity measure between I_{k-1} and $\mathbf{T}_{2D}^{k-1,k}(I_k)$

The homography $\mathbf{T}_{2D}^{k-1,k}$ determined with (13) is now used to superimpose image I_k on I_{k-1}. The hue being constant in bladder images [22], the pixel values of I_k and I_{k-1} are converted into grey-levels for the

$$\begin{bmatrix} x_{2D}^{1,k} & y_{2D}^{1,k} & 1 & 0 & 0 & 0 & -c_{1,1}^{k-1,k}x_{2D}^{1,k} & -c_{1,1}^{k-1,k}y_{2D}^{1,k} \\ 0 & 0 & 0 & x_{2D}^{1,k} & y_{2D}^{1,k} & 1 & -c_{2,1}^{k-1,k}x_{2D}^{1,k} & -c_{2,1}^{k-1,k}y_{2D}^{1,k} \\ \vdots & \vdots & \vdots & \vdots & \vdots & \vdots & \vdots & \vdots \\ x_{2D}^{M,k} & y_{2D}^{M,k} & 1 & 0 & 0 & 0 & -c_{1,M}^{k-1,k}x_{2D}^{M,k} & -c_{1,M}^{k-1,k}y_{2D}^{M,k} \\ 0 & 0 & 0 & x_{2D}^{M,k} & y_{2D}^{M,k} & 1 & -c_{2,M}^{k-1,k}x_{2D}^{M,k} & -c_{2,M}^{k-1,k}y_{2D}^{M,k} \end{bmatrix} \begin{bmatrix} a_{1,1}^{k-1,k} \\ a_{1,2}^{k-1,k} \\ a_{1,3}^{k-1,k} \\ a_{2,1}^{k-1,k} \\ a_{2,2}^{k-1,k} \\ a_{2,3}^{k-1,k} \\ a_{3,1}^{k-1,k} \\ a_{3,2}^{k-1,k} \end{bmatrix} = \begin{bmatrix} c_{1,1}^{k-1,k} \\ c_{2,1}^{k-1,k} \\ \vdots \\ c_{1,M}^{k-1,k} \\ c_{2,M}^{k-1,k} \end{bmatrix} \tag{13}$$

Algorithm 1: Data registration of viewpoints k and $k-1$.

Input:
- Source image I_k and target image I_{k-1}.
- M laser points of viewpoint k given in 3D and 2D: $\{P_{3D}^{i,k},\ P_{2D}^{i,k}\}|_{i\in\{1,\ldots,M\}}$.
- Initial simplex given in (16), and related similarity values $\varepsilon(V_e)$, $e \in \{1,\ldots,7\}$.

Output: Geometrical transformation linking viewpoints k and $k-1$:
- homography matrix $\mathbf{T}_{2D}^{k-1,k}$.
- translation vector $D^{k-1,k}$ and angles $\theta_1^{k-1,k}$, $\theta_2^{k-1,k}$ and $\theta_3^{k-1,k}$ induced by the estimated 3×4 rigid transformation matrix $\mathbf{T}_{3D}^{k-1,k}$.

repeat
- *Step 1*: Replace the vertex of smallest $\varepsilon(V_e)$ value by a new vertex according to the symmetry rules of the simplex algorithm. Then, update the entries of $\mathbf{T}_{3D}^{k-1,k}$ (see (3)) from the knowledge of $\theta_1^{k-1,k}$, $\theta_2^{k-1,k}$, $\theta_3^{k-1,k}$, and of the 3D translation vector $D^{k-1,k}$ for the new vertex;
- *Step 2*: Given (13) and the M points $(P_{3D}^{i,k}, P_{2D}^{i,k})$, compute the 8 parameters of the homography $\mathbf{T}_{2D}^{k-1,k}$ induced by the rigid transformation $\mathbf{T}_{3D}^{k-1,k}$ determined in *Step 1*;
- *Step 3*: Superimpose I_k on I_{k-1} using (5) and the homography $\mathbf{T}_{2D}^{k-1,k}$ obtained in *step 2*;
- *Step 4*: For the new vertex, assess the registration quality $\varepsilon(V_e)$ using (15) and the images superimposed in *step 3*;

until *the variation of the simplex volume leads to a mean displacement value of* I_k *on* $I_{k-1} < 0.1$ *pixel*;

Store the six parameters of the vertex having the largest $\varepsilon(V_e)$ value in $D^{k-1,k}$, $\theta_1^{k-1,k}$, $\theta_2^{k-1,k}$, and $\theta_3^{k-1,k}$;
Fill matrix $\mathbf{T}_{3D}^{k-1,k}$ with the rigid transformation parameters computed from $D^{k-1,k}$, $\theta_1^{k-1,k}$, $\theta_2^{k-1,k}$, and $\theta_3^{k-1,k}$: see (3);
Fill matrix $\mathbf{T}_{2D}^{k-1,k}$ with the homography parameters corresponding to $\mathbf{T}_{3D}^{k-1,k}$.

registration step. As shown in [17], homologous features cannot be systematically extracted from the images due to blur, weak textures or lacking textures in some image parts. Therefore, iconic data are directly used to measure the similarity of the overlapping parts of I_k and I_{k-1}. The mutual information, denoted by $\mathcal{MI}(I_{k-1}, \mathbf{T}_{2D}^{k-1,k}(I_k))$, is a robust similarity measure [26] which was successfully used for 2D bladder image mosaicing [22]. This statistical measure is notably robust since it is computed with the whole pixels of the common regions of the superimposed images. The mutual information is defined from the grey-level entropies $\mathcal{H}(I_{k-1})$ and $\mathcal{H}(\mathbf{T}_{2D}^{k-1,k}(I_k))$ and the joint grey-level entropy $\mathcal{H}_J(I_{k-1}, \mathbf{T}_{2D}^{k-1,k}(I_k))$ of source image I_k and target image I_{k-1}:

$$\mathcal{MI}\left(I_{k-1}, \mathbf{T}_{2D}^{k-1,k}(I_k)\right) = \mathcal{H}(I_{k-1}) + \mathcal{H}(\mathbf{T}_{2D}^{k-1,k}(I_k)) - \mathcal{H}_J(I_{k-1}, \mathbf{T}_{2D}^{k-1,k}(I_k)) \quad (14)$$

with

$$\begin{cases} \mathcal{H}(I_{k-1}) = -\sum\limits_{z_{k-1}} p(z_{k-1}) \log p(z_{k-1}) \\ \mathcal{H}(\mathbf{T}_{2D}^{k-1,k}(I_k)) = -\sum\limits_{z_k} p(z_k) \log p(z_k) \\ \mathcal{H}_J(I_{k-1}, \mathbf{T}_{2D}^{k-1,k}(I_k)) = \\ \qquad -\sum\limits_{z_{k-1}} \sum\limits_{z_k} p_J(z_{k-1}, z_k) \log p_J(z_{k-1}, z_k). \end{cases}$$

The grey-levels z_{k-1} and z_k range in $[0, 255]$ because images are single-byte encoded. $p(z_{k-1})$ and $p(z_k)$ are the probability density functions of the overlapping parts of images I_{k-1} and $\mathbf{T}_{2D}^{k-1,k}(I_k)$ whereas $p_J(z_{k-1}, z_k)$ is a joint probability density function. The mutual information is maximal when both images are registered, *i.e.*, when I_{k-1} is statistically correlated with $\mathbf{T}_{2D}^{k-1,k}(I_k)$.

3.2.4 Registration algorithm

The mutual information is maximized with respect to the rotation angles $\theta_1^{k-1,k}$, $\theta_2^{k-1,k}$, $\theta_3^{k-1,k}$ and the translation parameter $D^{k-1,k}$ appearing in (3). The optimization task is done using the simplex algorithm [24] since the cost function (14) is non-differentiable. Because there are six unknowns, the simplex is composed of seven vertices V_e (with $e \in \{1,\ldots,7\}$) lying in $\mathbb{R}^6$. The similarity measure

$$\varepsilon(V_e) = \mathcal{MI}(I_{k-1}, \mathbf{T}_{2D}^{k-1,k}(I_k)) \quad (15)$$

is computed for each vertex V_e, where the $\mathbf{T}_{2D}^{k-1,k}$ matrix deduces from V_e as detailed in § 3.2.2. At each iteration, the vertex of smallest $\varepsilon(V_e)$ value is replaced by a new vertex whose location in the parameter space is computed with the simplex symmetry rules. The angles and translations associated to the new vertex are used to determine the rigid transformation matrix, compute the related homography matrix, and then measure the image registration quality using (15). By repeating this process, the simplex vertices gradually converge towards the maximizer of (14). The optimization principle is detailed in Algorithm 1. The initial simplex size is experimentally set relative to the 25 images/s acquisi-

tion rate and the low cystoscope speed, leading to submillimetric translations and to rotations smaller than 1° between two acquisitions. The universal initial simplex is built with 0.3 mm translations and 0.4° rotation values:

$$\begin{array}{l} V_1 = [0 \quad 0 \quad 0 \quad 0 \quad 0 \quad 0] \\ V_2 = [0.3 \quad 0 \quad 0 \quad 0 \quad 0 \quad 0] \\ V_3 = [0 \quad 0.3 \quad 0 \quad 0 \quad 0 \quad 0] \\ V_4 = [0 \quad 0 \quad 0.3 \quad 0 \quad 0 \quad 0] \\ V_5 = [0 \quad 0 \quad 0 \quad 0.4 \quad 0 \quad 0] \\ V_6 = [0 \quad 0 \quad 0 \quad 0 \quad 0.4 \quad 0] \\ V_7 = [0 \quad 0 \quad 0 \quad 0 \quad 0 \quad 0.4] \end{array} \tag{16}$$

Each vertex gathers the three translation parameters (first three entries in D), and then θ_1, θ_2 and θ_3. The iterative process of Algorithm 1 is stopped when the mean displacement of the corners of image I_k (displaced in the I_{k-1} domain) becomes smaller than 0.1 pixel. When the optimization task is completed, the geometrical links between consecutive coordinate systems $\{c_k\}$ and $\{c_{k-1}\}$ and consecutive images (I_k, I_{k-1}) are fully defined by $\mathbf{T}_{3D}^{k-1,k}$ and $\mathbf{T}_{2D}^{k-1,k}$, respectively.

3.3 Data mosaicing

The 3D laser points from all viewpoints k have to be expressed in a common coordinate system. Choosing the camera coordinate system of the first acquisition, the points of viewpoint k are displaced from $\{c_k\}$ to $\{c_1\}$ using the "global" (g) transformation matrix:

$$\mathbf{T}_{3D}^{k,g} = \prod_{j=2}^{k} \mathbf{T}_{3D}^{j-1,j} = \mathbf{T}_{3D}^{1,2} \times \mathbf{T}_{3D}^{2,3} \times \ldots \times \mathbf{T}_{3D}^{k-1,k}. \tag{17}$$

The whole set of points in $\{c_1\}$ is then exploited to compute a 3D mesh with triangular faces representing the bladder surface [20]. Finally, the textures of images I_k can be projected onto the 3D mesh. Specifically, the color of each triangular face in the 3D mesh is obtained by copying the color of the pixel in the first image of the video in which the triangular face can be seen. This simple choice could be improved using more involved strategies in order to reduce possible texture discontinuities in the 3D mosaic or to smooth the 3D surface by thin-plate interpolation. See *e.g.*, [29] in the 2D case.

Similar to the 3D case, a 2D mosaic is built by taking the coordinate system of the first image as reference and using the global 2D matrices:

$$\mathbf{T}_{2D}^{k,g} = \prod_{j=2}^{k} \mathbf{T}_{2D}^{j-1,j} = \mathbf{T}_{2D}^{1,2} \times \mathbf{T}_{2D}^{2,3} \times \ldots \times \mathbf{T}_{2D}^{k-1,k}. \tag{18}$$

It has to be noticed that the green laser points cover a small surface in the images and are easy to segment since a simple thresholding of the H (hue) component in the HSV color space robustly separates the green laser points from the reddish or orange bladder epithelium pixels (see [16] for a detailed description of the HSV color space family). Since images I_k and I_{k-1} include large common scene parts, the missing bladder textures in I_{k-1} can be replaced in the mosaic by the homologous texture pixels of I_k. The correspondence between pixel textures hidden by laser dots in image I_{k-1} and the corresponding visible texture pixels in image I_k is given by homography $T_{2D}^{k-1,k}$. This correspondence is used to build 2D and 3D mosaics without laser dot pixels.

4 Quantitative results for prototype data

The goal of this section is to validate on real data that the mosaicing approach of Section 3 indeed leads to coherent surface construction results. To do so, an active vision prototype is first proposed. Then, 3D mosaicing results are presented for data acquired with the prototype using three real phantoms, on which pig bladder texture images were stuck. This allows for a first quantitative assessment of the mosaicing accuracy based on ground truths. As mentioned before, our prototype cannot be used in clinical situations yet. It was rather designed for validation of the structured-light approach in combination with a cystoscope and to show the feasibility of 3D cartography. The applicability to clinical situations will be further discussed in Sections 5 and 7 together with complementary tests on realistic simulated data.

4.1 Prototype and test phantom description

Our active vision prototype is illustrated in Fig. 3. The acquisition channel consists of a Karl Storz cystoscope, and the image sequences are acquired with a Basler scout model camera. The image resolution is 768 × 576 pixels. The diffractive lens is fixed nearby the wide FOV lens of the cystoscope distal tip. The principle of the laser ray projection is sketched in Fig. 3(a). This prototype uses the triangulation principle described in Section 2 and has a geometry equivalent to that of Fig. 2(a). The baseline (distance between the camera and projector optical centers, see Fig. 3(a)) available for triangulation is about 3 mm. The laser projector wavelength is equal to 520 nm, and the 10 mW power should be adapted for further clinical deployment.

High resolution images of an incised and flattened pig bladder were acquired to simulate human bladder textures (see Fig. 4(b)). The images were printed on paper sheets and stuck on surfaces with various shapes.

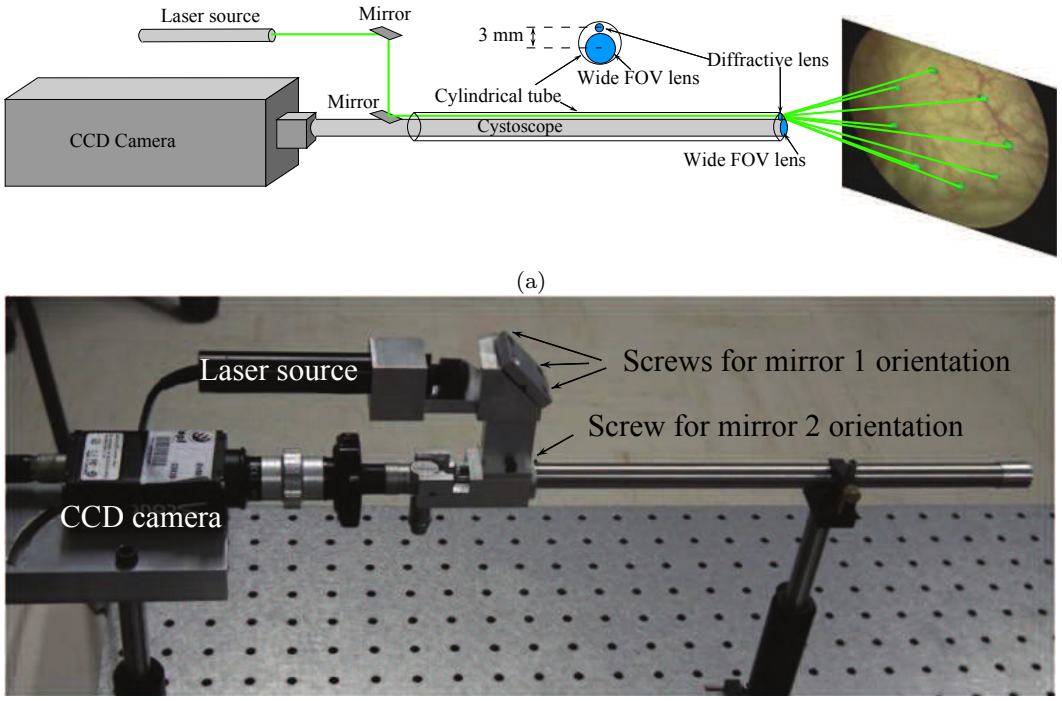

Fig. 3 Active vision prototype. (a) Principle of the structured-light prototype. The trajectory of the beam emitted by the laser source is precisely controlled by two mirrors. The adjustable mirror orientations ensure that the laser beam falls on the center of the diffractive lens. This lens projects eight laser rays onto the scene. The laser wavelength and power were set to 532 nm and 10 mW. The green color allows us to have a good contrast between the image textures and the green laser points. The 10 mW power was actually much too strong, therefore optical attenuators were used. The triangulation principle is sketched in Fig. 2 and described in Section 2. The prototype (camera and projector) was calibrated using the generic method described in [10]. (b) Prototype corresponding to the sketch in (a). Mirrors 1 and 2 are fixed onto planar metal supports. The orientation of the planar supports is precisely set using three screws. The planar support and two screws are not visible for mirror 2.

Fig. 4 Three real phantoms. The planar phantom (a) is used to assess the accuracy of the 3D registration algorithm. The half cylinder (b) and wave (c) phantoms allow us to evaluate the ability of the registration method to construct convex and nonconvex surface parts, respectively.

First, the planar surface of Fig. 4(a) is used to test the 3D mosaicing algorithm. Here, the underlying assumption in the proposed algorithm is perfectly fulfilled: the surfaces viewed in consecutive images are planar. Then, the half cylinder of Fig. 4(b) is used to simulate a convex surface. The half cylinder has a radius of 35 mm and allows for simulating a plausible bladder curvature in the direction orthogonal to the main cylinder axis (a non-warped bladder can be approximately thought of as an ellipsoid with a major axis from 80 to 100 mm and minor axes from 30 to 40 mm). The bladder is in contact with other organs is often warped. In this case, the surface includes concave parts due to troughs in the organ wall. As shown in Fig. 4(c), a wave phantom was built to simulate warped bladder parts with troughs between waves. The length of the wave (a period of the phan-

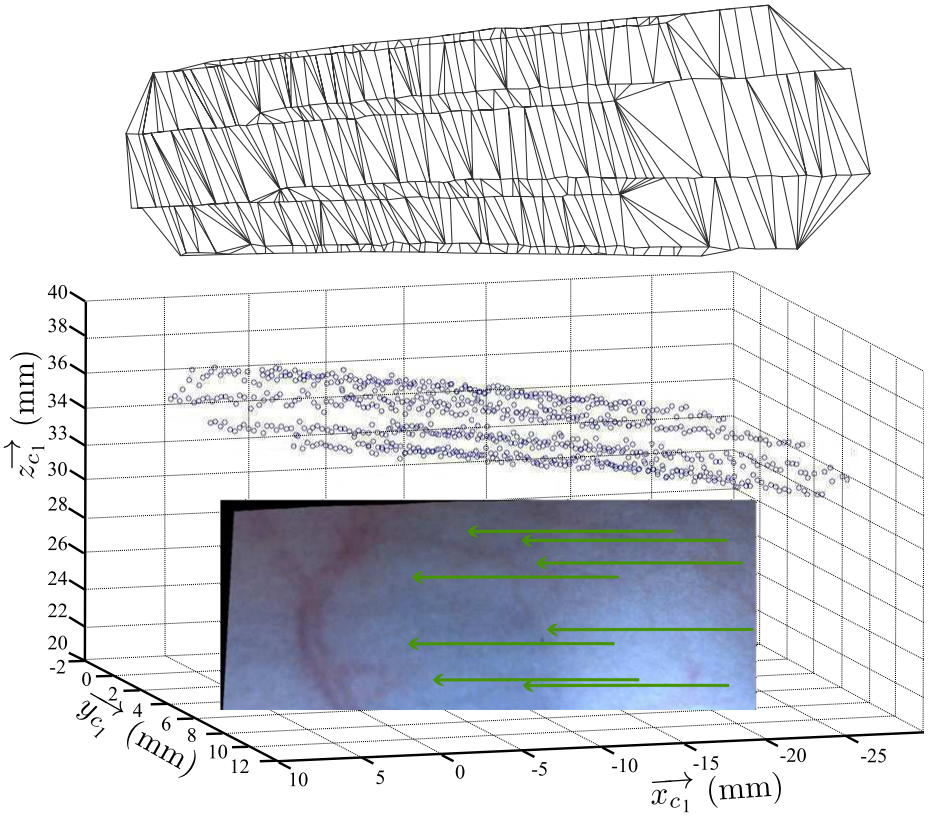

Fig. 5 Plane construction results. Bottom: 2D mosaic. The green arrows refer to the 8 laser point displacements (constant translation, no rotation) throughout image acquisition. Center: 3D points placed in the common coordinate system $(O_{c_1}, \overrightarrow{x_{c_1}}, \overrightarrow{y_{c_1}}, \overrightarrow{z_{c_1}})$. Top: related mesh with triangular faces on which the 2D mosaic image can be projected.

tom) is 40 mm and the wave depth (from the trough to the crest of the wave) is 20 mm. This phantom simulates extreme situations since consecutive troughs of large magnitude never arise in practice. All phantoms are positioned and displaced relative to the endoscope prototype using a micrometric positioning table to generate ground truth 3D transformations.

4.2 Point reconstruction accuracy and surface construction results

Once the prototype has been calibrated with the method described in [10], 3D point reconstruction is performed in the local camera coordinate system $\{c_k\}$, and $M = 8$ $P_{3D}^{i,k}$ points are then available per viewpoint k.

In order to evaluate the laser point reconstruction accuracy, a first data acquisition was carried out using the wave phantom. The cystoscope axis was held orthogonal to the translation plane and $K = 200$ images were acquired with 1 mm translation steps. The range of z_{c_k}-values that were found (in between 20 and 40 mm) for the $P_{3D}^{i,k}$ points matches the wave height, equal to 20 mm. It was further verified that for prototype distal tip-to-surface distances ranging from some millimeters to 5 centimeters, the average reconstruction error on the z_{c_k} coordinate (depth) is close to 0.5 mm and remains submillimetric for all points. When normalizing this 3D reconstruction error by the tip-to-surface distance, the errors are always lower than 3 %. This accuracy is by far sufficient for bladder surface mosaicing since the constructed surface shape must only be representative of the organ wall (a precise dimensional measure does not make sense in urology).

In the following surface construction tests and without loss of generality, the phantoms were displaced in front of the fixed prototype. This is in contrast with the setup of Section 3, where the instrument is moving inside the organ. However, it is easy to see that the proposed mosaicing algorithm remains valid and unchanged in both settings whatever the moving object (surface or instrument). The simultaneous 2D and 3D data mosaicing results are illustrated in Fig. 5 for the planar phantom. Here, 100 images were acquired for 99 constant translations of 0.3 mm (with the three components of $D^{k-1,k}$ different from 0) and without 3D rotations. Thus, the magnitude of 3D displacements is equal to:

$$\|D^{k-1,k}\| = 0.3 \tag{19}$$

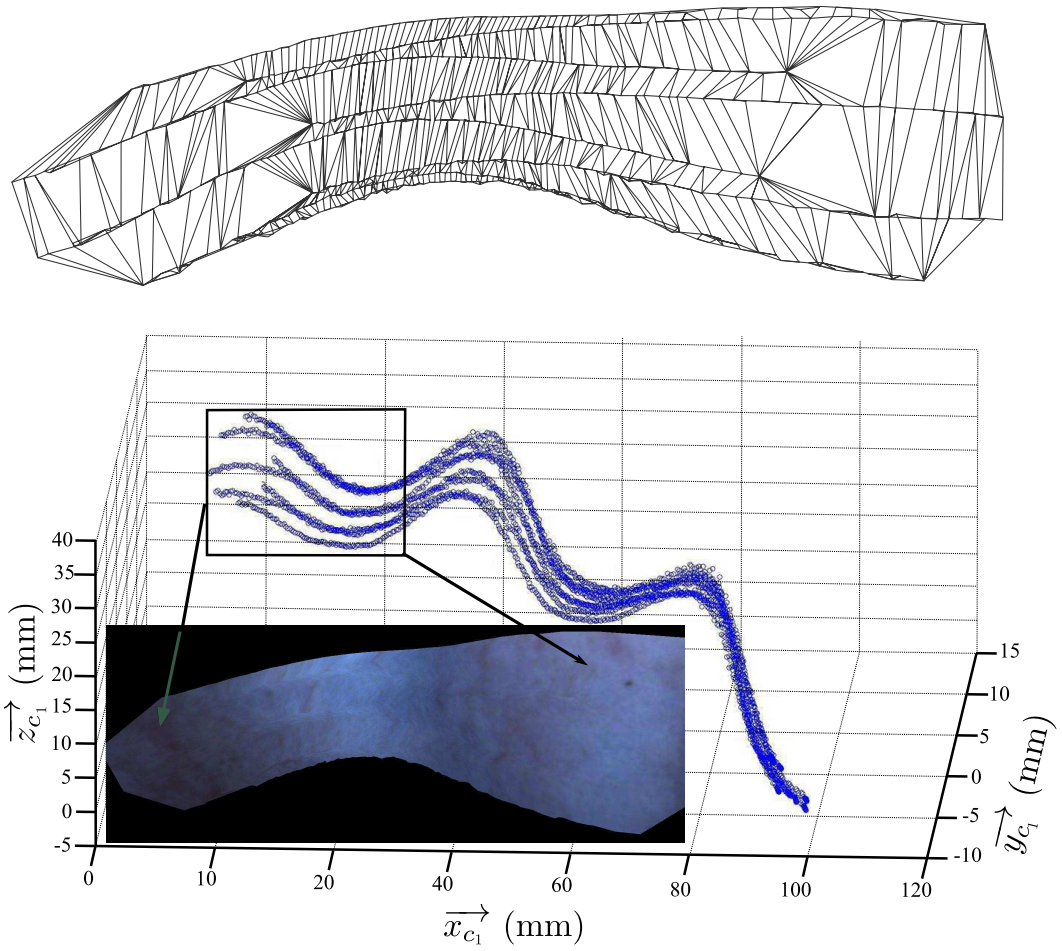

Fig. 6 Wave construction results. Center: 3D points placed in the common camera coordinate system $(O_{c_1}, \overrightarrow{x_{c_1}}, \overrightarrow{y_{c_1}}, \overrightarrow{z_{c_1}})$ and representing 2.5 wave periods in the phantom of Fig. 4(c). Top: mesh surface reconstructed from the first 100 acquisitions (zoom in rectangle). Bottom: textured surface corresponding to the first 100 acquisitions. The cystoscope prototype is roughly oriented along the $\overrightarrow{z_{c_1}}$ axis. The local phantom surface corresponding to the left edge of the zoom in rectangle is the most distant from the camera in contrast with the local surface related to the right edge.

where $\|\,.\,\|$ stands for the Euclidean norm.

The average translation magnitude and standard deviation computed with the registration algorithm for the 99 consecutive image pairs are 0.27 ± 0.015 mm, whereas the angles $\theta_1^{k-1,k}$, $\theta_2^{k-1,k}$ and $\theta_3^{k-1,k}$ indeed tend towards 0°. So, the average magnitude of displacement is slightly underestimated with respect to the ground truth (0.3 mm), whereas the 0.015 mm standard deviation value is very low. These results are a first indication that the nature (translation) of the displacement can be successfully determined using the registration algorithm. Fig. 5 confirms that accurate results are obtained for the planar phantom. The 2D mosaic built from the estimated $\mathbf{T}_{2D}^{k-1,k}$ homographies is visually coherent, *i.e.*, without texture discontinuities between images. In the textured image of Fig. 5, the green arrows represent the trajectory of the eight laser points throughout the video-image acquisition. As could be expected, these trajectories are affine because the camera movement is a pure translation. The 3D points, placed in the common coordinate system $\{c_1\}$, all lie on a plane. The constructed mesh with triangular faces is displayed in the top image of Fig. 5.

In the following surface construction tests, we aim to address a case where the geometrical link between the surfaces in the FOV of two images is not exactly an homography (working assumption of the 3D registration algorithm) since the local surfaces are not planar anymore. The data of Fig. 6 were acquired for the wave phantom with the same displacements as before: acquisition of $K = 360$ images for 359 constant translations of 0.3 mm and without any rotation. For this phantom, the local surface orientation with respect to the cystoscope optical axis strongly varies throughout the sequence. To quantify the algorithm accuracy, we used again criterion (19). The average magnitude of the 3D translations computed with the registration algorithm for consecutive image pairs is 0.29 ± 0.03 mm,

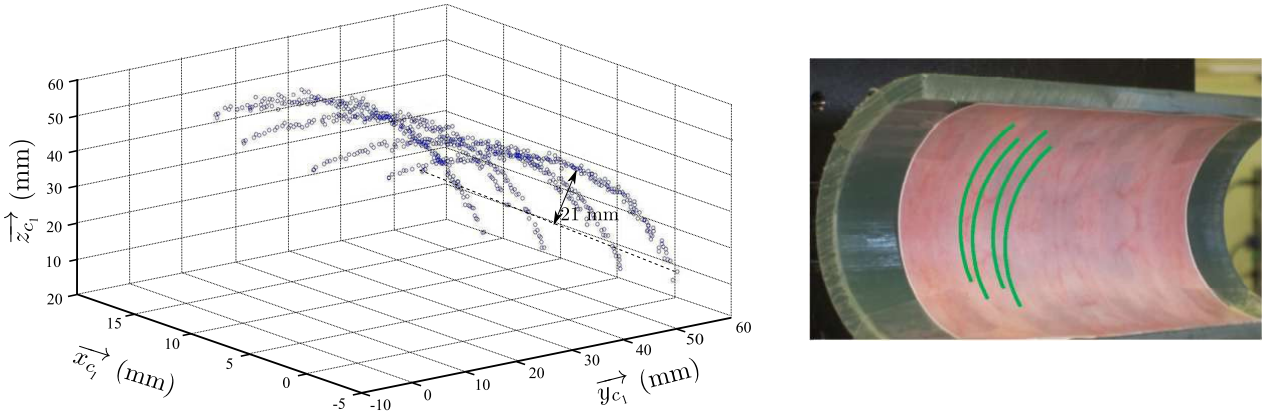

(a) (b)

Fig. 7 Half cylinder reconstruction results. (a) 3D points placed in the global coordinate system $\{c_1\}$. Their locations are consistent with the trajectories sketched in green on the half cylinder phantom (b). Each green curve represents the trajectory of two very close laser points.

and $\theta_1^{k-1,k} = \theta_2^{k-1,k} = \theta_3^{k-1,k} \approx 0°$. The magnitude of translations (0.29 mm) is very close to the true average displacement (0.3 mm) whereas the related standard deviation (0.03 mm) remains very close to the ideal zero value. These results show that the translation of the cystoscope prototype can be successfully determined for non-planar surfaces and for varying angles between the local surface and the cystoscope optical axis. The variation of this angle combined with changes of phantom-to-camera distances (see Fig. 6) impact the perspective ($a_{3,1}^{k-1,k}$ and $a_{3,2}^{k-1,k}$), shearing ($s_x^{k-1,k}$ and $s_y^{k-1,k}$), and scale ($\alpha^{k-1,k}$) parameters, see (4).

The blue points in Fig. 6 represent again the 3D laser points placed in the common coordinate system $(O_{c_1}, \overrightarrow{x_{c_1}}, \overrightarrow{y_{c_1}}, \overrightarrow{z_{c_1}})$. The 360 viewpoints correspond to 2.5 wave periods, *i.e.*, a length of 100 mm. Qualitatively, the global surface indeed corresponds to waves although after 1.5 wave period, the wave surface bends itself instead of remaining straight. However, the results are satisfactory since a wave period represents an organ pushing against the bladder (*e.g.*, a trough), and two or three consecutive troughs are an extreme situation never arising for cystoscopic data.

In Fig. 7, the cystoscope prototype was approximately held at a 30 mm distance from the half cylinder surface (of radius 190 mm) during the acquisition of 130 images. The surface covered by the cystoscope corresponds to a circular arc of aperture 130°. The displacements between consecutive acquisitions $k-1$ and k mainly consist of 1° rotations around $\overrightarrow{x_{c_1}}$ combined with small translations and rotations around $\overrightarrow{y_{c_1}}$ and $\overrightarrow{z_{c_1}}$. Fig. 7 shows that the reconstructed points indeed lay on a cylindrical surface. The depth of the cylinder part was used to quantify the surface construction accuracy. Ideally, the dashed line in Fig. 7(a) should circumscribe an arc of aperture 130°. The real depth of the cylinder part corresponding to the 130° phantom aperture is 25 mm, whereas the depth computed from the reconstructed data is 21 mm. This error does not alter the visual quality of the surface representation: the phantom shape is indeed cylindrical and no dimensional analysis is required.

4.3 Overview of the results related to prototype data

The results obtained so far are a first validation that the prototype displacement (*i.e.*, the displacement of the camera coordinate system in between two acquisitions) can be recovered using only the video-image and 8 laser points per acquisition. Indeed, for both phantom types, the deviation of the estimated 3D displacement from the ground truth is small.

- *Local surface planarity.* Planarity is one of the main differences between the plane and wave phantoms. Indeed, the planar assumption (made for registering two images using an homography) is not fulfilled anymore for the surface parts of the wave. We found that the camera displacements were computed with similar accuracy for both planar and non-planar surfaces. It was already proved in the frame of 2D bladder mosaicing that image registration with homographies is accurate even for regions where the bladder is non-planar [30] or contains lesions such as polyps [17]. The results of § 4.2 indicate that homographies linking 2D images are appropriate as well for 3D mosaicing.

- *3D point reconstruction accuracy.* Inaccurate 3D laser point reconstruction impacts the precision of 3D

camera displacement estimation. The results obtained with real phantoms show that 3D point reconstruction is accurate enough to enable camera motion assessment and 3D mosaicing, even for active vision prototypes having small baselines (3 mm here).

- *Cystoscope axis orientation.* For tests with wave phantoms, the angle between the cystoscope optical axis and the normal to the local surface is varying: at extreme points (points of minimum or maximum depth) of the wave, the angles are small ($\approx 0°$), whereas for medium points, their value is maximum (45°). The accuracy of the reconstructed camera displacement is not strongly impacted by the variation of angles.

The tests with the plane and wave phantoms involved 3D translations, whereas the viewpoint changes arising in the half-cylinder experiment combined both rotations and translations. In the latter case, no ground truth displacements were available. However, the cylinder depth that was estimated for an 130° aperture shows that the surface shape can be accurately recovered.

In all tests, images were acquired for a distal tip-to-surface distance ranging from 10 to 40 mm and for surface areas of one to several square centimetres. These dimensions are consistent with real bladder image acquisitions in terms of acquisition distance variation and size of the area viewed in images. For this distance interval, the laser points were systematically visible in the images, and their position could then be reconstructed in the camera coordinate system.

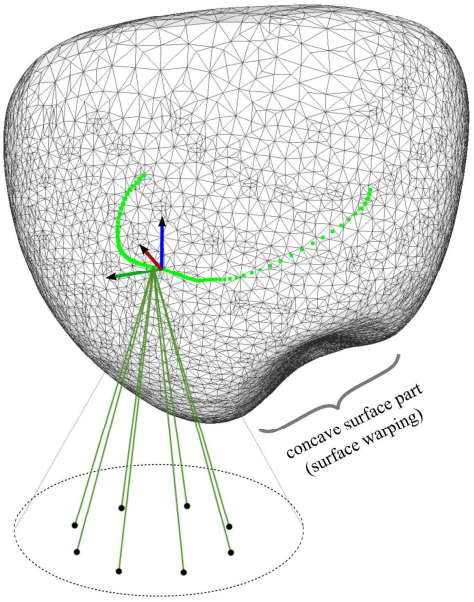

Fig. 8 Simulated bladder volume and simulation of video sequence acquisition with known 3D endoscope displacements. The cone corresponds to the field of view of the camera for one viewpoint. The green dashed curve refers to the trajectory of the virtual cystoscope. The simulated video sequence then contains images related to both convex and nonconvex parts of the virtual bladder.

5 Results for realistic simulated data

The results presented so far are a first validation of the feasibility of 3D bladder mosaicing. However, similar to the contributions of Soper *et al* [28] and Shevchenko *et al* [27], the method was not tested on patient data (our active vision prototype was not built for patient data acquisition at this stage). In this section, realistic bladder data are simulated to perform complementary mosaicing tests. Not only the bladder volume and texture are closer to human data, but also the simulated endoscope trajectory can be controlled to reproduce all types of cystoscope displacements.

5.1 Simulation of textured bladder data

To simulate a more realistic bladder shape, we considered a (convex) oval volume whose width, height and depth are equal to 110, 100, and 70 mm, respectively (the standard capacity/volume of the bladder ranges in between 400 and 600 ml). The ovoid was then locally deformed to create a nonconvex surface part. This surface, illustrated in Fig. 8, was defined in agreement with the Institut de Cancérologie de Lorraine. Human bladder textures were extracted from large FOV mosaics built using 2D mosaicing algorithms [22,30]. Three such mosaics were considered (see Fig. 1) and mapped on the inner wall of the simulated 3D bladder surface.

Blender (a 3D graphics modeling and rendering software [13]) was used to simulate the camera and the laser projector while reproducing the geometrical configuration of our prototype. Such 3D representation can be found in Fig. 8. Both camera and laser projector parameters (calibrated using [10]) are handled. Moreover, Blender allows us to simulate complex cystoscope trajectories combining rotations and translations. Similar to clinical examinations, the distance between the cystoscope distal tip and the surface is changing. The resulting area seen in images varies from 1 to a few square centimeters. Fig. 9 displays a sample of the simulated video-sequences obtained for each of the three numerical phantoms using the 3D surface of Fig. 8. Each image sequence includes 120 images and covers 24 cm^2 of the phantom surface. Importantly, the texture variability is large from one video-sequence to another.

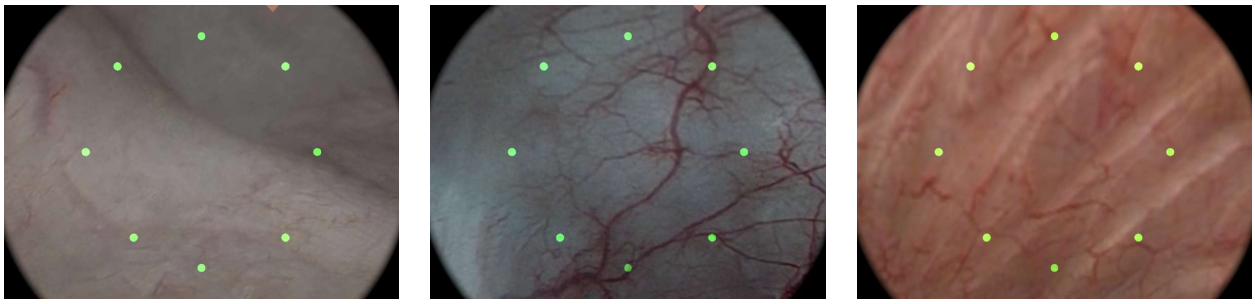

(a) (b) (c)

Fig. 9 Extraction of an image from each of the three simulated video-sequences. (a) Image with weakly contrasted texture. (b) Image with highly contrasted vessels. (c) Image with blurry texture.

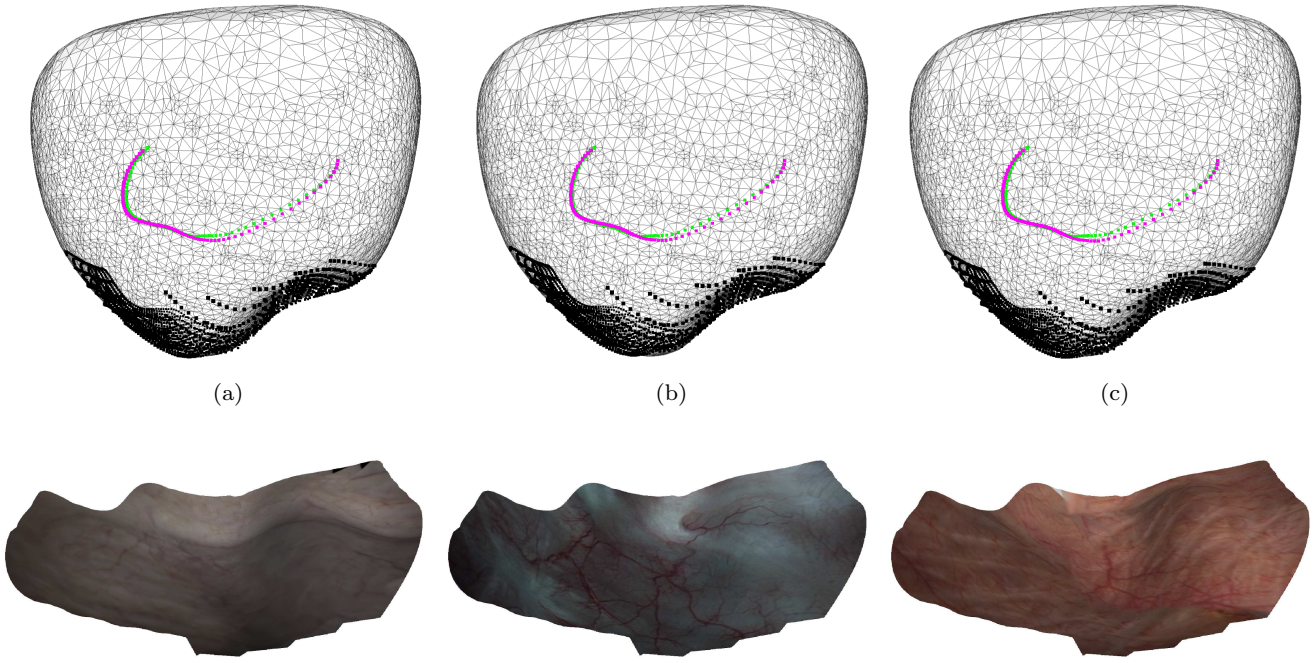

(a) (b) (c)

(d) (e) (f)

Fig. 10 Results obtained for the three numerical phantoms related to Fig. 9(a,b,c). Top: constructed 3D point cloud (in black) and cystoscope trajectory (magenta curve). The point cloud is displayed along with the ground truth surfaces (grey mesh) to visually assess their overlapping quality. The green dashed curve refers to the ground truth cystoscope trajectory. For readability reasons, the meshed surface generated from the reconstructed 3D points is not shown. Bottom: 3D reconstructed mosaics seen from above (for improved readability).

5.2 Surface construction results for the simulated data

The proposed 3D mosaicing method was applied to the three simulated data sequences. Fig. 10(a,b,c) displays the cloud of reconstructed points $P_{3D}^{i,k}$ for each sequence in the common coordinate system $\{c_1\}$ together with the trajectory of the optical center of the cystoscope prototype (the computed trajectory appears in magenta). The textured surfaces generated from the cloud of 3D points can be found in Fig. 10(d,e,f).

The surface construction accuracy is assessed by computing the average Euclidean distance between the reconstructed 3D points in $\{c_1\}$ and their ground truth locations on the phantom surface. These distances are ideally equal to 0. The numerical errors obtained for the three phantoms are 0.79±0.34 mm, 0.78±0.33 mm, and 0.80±0.34 mm, respectively. On Fig. 10, it is noticeable that the shape of the reconstructed surface part (containing the black points) is visually consistent with that of the true surface (grey mesh). The mean error is small (< 1 mm), confirming that the reconstructed extended FOV surfaces remain accurate for both convex and nonconvex surface parts.

Phantom type	Planar phantom (Fig. 5)	Wave phantom (Fig. 6)	First numerical phantom (Fig. 10(a))	Second numerical phantom (Fig. 10(b))	Third numerical phantom (Fig. 10(c))
Mean $\epsilon_{3D}^{k-1,k}$	0.016±0.002	0.05±0.01	0.021± 0.0023	0.023± 0.0025	0.023±0.0027
Mean $\epsilon_{2D}^{k-1,k}$	0.30±0.29	0.85±0.8	0.40±0.39	0.42±0.37	0.43±0.39

Table 1 Registration errors for five phantoms. The mean (over k) and standard deviation ($mean \pm std$) of criteria $\epsilon_{3D}^{k-1,k}$ and $\epsilon_{2D}^{k-1,k}$ are in millimetres and pixels, respectively.

5.3 Discussion on the simulated data results

Several conclusions can be drawn. First, the bladder surface of Fig. 8 was accurately constructed for video-sequences containing various human textures. Second, the average 3D error remains small (less than 1 mm) in all cases. The proposed algorithm was also able to deal with the pig bladder textures (shown in Section 4), which is another indication of its robustness against bladder texture variations. The use of mutual information as a similarity measure is the main reason behind this robustness.

For long video sequences, it may occur that the 3D points $P_{3D}^{i,k}$ substantially diverge from the ground truth surface. This is due to the accumulation of 3D registration errors over the sequence. Error accumulation is a common issue when 2D or 3D transformations between consecutive frames are sequentially estimated. This problem was already encountered for 2D mosaicing algorithms, and efficient solutions were proposed, based on a global texture discontinuity correction over the processed image sequence [30].

6 Assessment of registration accuracy

The quantitative results of Sections 4.2 and 5.2 are respectively related to the accuracy of the endoscope displacement and surface estimation. This section focusses on the registration accuracy between viewpoints.

6.1 Registration accuracy criteria

In (20), $\epsilon_{3D}^{k-1,k}$ defines the 3D registration error computed with the known ground truth transformation $\mathbf{T}_{3D,gt}^{k-1,k}$ and the transformation $\mathbf{T}_{3D}^{k-1,k}$ estimated with the proposed registration algorithm. Criterion $\epsilon_{3D}^{k-1,k}$ computes the mean Euclidean distance in millimetres between the exact and estimated locations of points $P_{3D}^{k,i}$, displaced in the coordinate system $\{c_{k-1}\}$ of viewpoint $k-1$:

$$\epsilon_{3D}^{k-1,k} = \frac{1}{N}\sum_{i=1}^{N}\left\|\hat{P}_{3D,gt}^{i,k-1} - \hat{P}_{3D}^{i,k-1}\right\| \quad (20)$$

where the displaced locations are respectively denoted by $\hat{P}_{3D,gt}^{i,k-1}$ and $\hat{P}_{3D}^{i,k-1}$. They are computed from $\hat{P}_{3D}^{i,k}$ using the ground truth and estimated transformations $\mathbf{T}_{3D,gt}^{k-1,k}$ and $\mathbf{T}_{3D}^{k-1,k}$; see (2). Ideally, $\epsilon_{3D}^{k-1,k}$ equals 0.

Similarly, in (21), criterion $\epsilon_{2D}^{k-1,k}$ computes the mean Euclidean distance in pixels between the projections in image I_{k-1} of the displaced 3D points $\hat{P}_{3D,gt}^{i,k-1}$ and $\hat{P}_{3D}^{i,k-1}$:

$$\epsilon_{2D}^{k-1,k}=\frac{1}{N}\sum_{i=1}^{N}\left\|\frac{1}{\hat{z}_{3D,gt}^{i,k-1}}\mathbf{K}\hat{P}_{3D,gt}^{i,k-1} - \frac{1}{\hat{z}_{3D}^{i,k-1}}\mathbf{K}\hat{P}_{3D}^{i,k-1}\right\| \quad (21)$$

$\mathbf{K}\hat{P}_{3D,gt}^{i,k-1}/\hat{z}_{3D,gt}^{i,k-1}$ and $\mathbf{K}\hat{P}_{3D}^{i,k-1}/\hat{z}_{3D}^{i,k-1}$ gather the coordinates in pixel unit of the ground truth and estimated point locations, where $\mathbf{K}$ is the projective matrix coding for the intrinsic camera parameters; see (1). Ideally, $\epsilon_{2D}^{k-1,k}$ also equals 0.

6.2 Registration results and accuracy discussion

Table 1 gives the registration errors, *i.e.*, the mean and standard deviation of the $\epsilon_{3D}^{k-1,k}$ and $\epsilon_{2D}^{k-1,k}$ values computed with the data of viewpoint pairs $(k-1,\ k)$ for five phantoms.

The results obtained for the planar phantom correspond to the inherent accuracy of the algorithm (best possible registration results obtained with the planarity assumption perfectly fulfilled). The mean (0.016 mm) and standard deviation (0.003 mm) of the $\epsilon_{3D}^{k-1,k}$ values show that in such ideal situation, the 3D registration errors between viewpoints are indeed very small. The 2D sub-pixel registration error is $\epsilon_{2D}^{k-1,k} = 0.30 \pm 0.29$ pixels for the planar phantom.

The planarity assumption is not fulfilled for the wave phantom: the field of view of the images is wide and visualizes large wave parts whose surfaces strongly deviate from a planar shape. In such an extreme situation, the mean registration error remains small (0.05 mm). Due to these small 3D registration errors, the surface in Fig. 6 has a correct global wave shape. Moreover, when scanning the wave surface, the angle between the 3D cystoscope prototype and the normal to the local surface takes values ranging in the whole interval [0-45] degrees. The small standard deviation of criterion

$\epsilon_{3D}^{k-1,k}$ (0.01 mm) indicates that the registration algorithm is robust towards changes of viewing angle. The mean of the 2D registration error (0.85 pixels) remains also small.

The 2D and 3D registration errors are quite close for all three numerical phantoms. The unique difference in the three numerical phantoms was the human bladder texture used for the data acquisition simulations (the surface shape and cystoscope trajectory was the same for all simulations). These results show that the registration algorithm is robust towards human bladder texture variability (the mutual information based similarity measure systematically led to comparable registration accuracy).

The $\epsilon_{3D}^{k-1,k}$ errors measured for the simulated phantoms are always larger than the $\epsilon_{3D}^{k-1,k}$ score obtained for the planar phantom (most favorable situation) and smaller than the $\epsilon_{3D}^{k-1,k}$ score for the wave phantom (most difficult situation). This is consistent with the fact that the phantom of Fig. 5 is exactly planar, the wave phantom is highly non-planar, whereas the degree of planarity of the numerical phantoms is intermediate. We would like to stress that the $\epsilon_{3D}^{k-1,k}$ and $\epsilon_{2D}^{k-1,k}$ scores obtained for the simulated phantoms are significantly closer to the error obtained for the plane rather than those of the wave phantom. This is an indication of the ability of the algorithm to reconstruct bladder shapes.

7 Conclusion

The proposed 3D bladder mosaicing algorithm is guided by 2D image registration. One advantage of the proposed approach is that no strong assumption is made on surface shapes. On the one hand, the choice of some initial surface shape is not required. On the other hand, smooth surfaces with both convex and nonconvex parts can be accurately constructed, the latter corresponding to warped bladder parts. Furthermore, the results obtained for pig bladder data and human bladder images highlight the robustness of the approach, since the mutual information based registration can cope with high texture variability.

An important feature of our endoscope prototype is that the triangulation geometry for 3D data acquisition and the baseline length of 3 mm are very close to those of the 3D cystoscopes which might be built for clinical use. A current trend in endoscopy is the "chip on the tip" technology (*i.e.*, sensors fixed on the distal tip of endoscopes). In this technology, the laser based solution can be used for both rigid and flexible cystoscopes (both the CCD matrix and the diffractive optics can be fixed on the distal tip): the calibration procedure described in [10] and the mosaicing algorithm proposed here remain unchanged. For rigid cystoscopes, the calibration and 3D point reconstruction methods are the same for different lens orientations (0° straight looking lens, 30° forward-oblique looking lens or 70° lateral looking lens).

Except for the optics to be implemented on the cystoscope for 3D point reconstruction, the modifications to be done for clinical translation are rather light. This is a key advantage over alternative solutions which rely on external devices [27,1]. This should lead to a drastic reduction of the overall cost of cystoscopy equipment together with a simplification of the technical installations in the examination rooms. Actually, the "chip on the tip" technology should allow us to simplify the prototype in future years: the cylindrical tube of Fig. 3 cannot be used in clinical situations, and it will not be used anymore.

Prior to the construction of a 3D cystoscope usable in clinical situation, it was required to validate both the measurement principle and the mosaicing algorithm on phantoms. Our work is the first which shows on phantoms with realistic bladder textures that 3D cystoscopy and mosaicing is feasible while minimally modifying standard endoscopes. This result is an important step in the process towards clinical 3D cystoscopy.

The proposed mosaicing algorithm may be improved in several situations.

1) When cystoscope trajectories are crossing, texture and 3D surface misalignments will be visible in the mosaic due to small error accumulation during the mosaicing process. Such crossings have to be automatically detected so that the surface, texture and color discontinuities can be corrected. Global 2D mosaic correction methods (such as the one proposed in [30]) may be adapted to improve the visual quality of 3D textured surfaces, but such approaches will not improve the 3D mosaics from the dimensional (accuracy) point of view.

2) It was shown in recent studies [3,4] that optical flow can provide an accurate dense correspondence between homologous points of bladder images with strong illuminations variations, large displacements or perspective changes, blur or weak textures. Thus, a perspective of this work is to elaborate an optical flow method with energies allowing for simultaneous optimization of the vector field and the parameters of the transformation $T_{3D}^{k-1,k}$.

3) The implementation of our algorithm may be improved as well in specific cases. When texture features are available and well spread over the images, they can be fastly detected [5]. Then, the distance between homologous texture points can be used as a similarity

measure for a given $\mathbf{T}_{2D}^{k-1,k}$, instead of the mutual information in (14).

When textures are lacking as in Fig. 1, the mutual information has to be used. Second, the processing time can obviously be reduced by replacing the sequential implementation of image registration (viewpoints $k-1$ and k for $k = 1, 2, \ldots$) by a parallel implementation *e.g.*, on a GPU graphical card. By coupling fast implementations with future clinical endoscopes based on the current proof-of-concept, we expect that the image processing time will remain moderate as compared to the times for acquiring images, for file transfers, and for archiving and retrieving data.

The registration algorithm was designed for bladder lesion diagnosis. It can be adapted to minimal invasive surgery in the abdominal cavity, *e.g.*, for computing extended FOV surfaces of the stomach. Indeed, the external stomach wall is smooth and contains textures close to bladder textures. Moreover, a laparoscope associated to a structured-light projector can be calibrated similar to a cystoscope. Increasing the FOV and providing 3D information facilitates a surgical intervention. For this application, real-time mosaicing must be reached.

Acknowledgements This work was sponsored by the Région Lorraine and the Centre National de la Recherche Scientifique (CNRS) under contract PEPS Biotechno et Imagerie de la Santé. The authors would also like to thank the Centre Hospitalier Universitaire Nancy-Brabois for providing pig bladders and Prof. François Guillemin from the Institut de Cancérologie de Lorraine for his expertise in urology.

References

1. Agenant, T.M., Noordmans, H.J., Koomen, W., Bosch, J.L.: Real-time bladder lesion registration and navigation: A phantom study. PLoS ONE **8**(1), e54,348 (2013)
2. Alcaraz, A.: Bladder cancer: Highlights from 2006. European Urology Supplements **6**, 737–744 (2007)
3. Ali, S., Daul, C., Galbrun, E., Blondel, W.: Illumination invariant optical flow using neighborhood descriptors. Computer Vision and Image Understanding **145**, 95–110 (2016)
4. Ali, S., Daul, C., Galbrun, E., Guillemin, F., Blondel, W.: Anisotropic motion estimation on edge preserving Riesz wavelets for robust video mosaicing. Pattern Recognition **51**(C), 425–442 (2016)
5. Ali, S., Daul, C., Weibel, T., Blondel, W.: Fast mosaicing of cystoscopic images from dense correspondence: combined SURF and TV-L1 optical flow method. In: 20th IEEE International Conference on Image Processing, pp. 1291–1295. Melbourne, Australia (2013)
6. Behrens, A.: Creating panoramic images for bladder fluorescence endoscopy. Acta Polytechnica **48**(3), 50–54 (2008)
7. Behrens, A., Stehle, T., Gross, S., Aach, T.: Local and global panoramic imaging for fluorescence bladder endoscopy. In: 31st Int. Conf. of the IEEE Engineering in Medicine and Biology Society, pp. 6690–6693. Minneapolis, USA (2009)
8. Behrens, A., Uski, M., Stehle, T., Gross, S., Aach, T.: Intensity based multi-scale blending for panoramic images in fluorescence endoscopy. In: IEEE International Symposium on Biomedical Imaging, pp. 1305–1308. Rotterdam, Netherlands (2010)
9. Ben-Hamadou, A., Daul, C., Soussen, C., Rekik, A., Blondel, W.: A novel 3D surface construction approach: Application to three-dimensional endoscopic data. In: 17th IEEE Int. Conf. on Image Processing, pp. 4425–4428. Hong Kong (2010)
10. Ben-Hamadou, A., Soussen, C., Daul, C., blondel, W., Wolf, D.: Flexible calibration of structured-light systems projecting point patterns. Computer Vision and Image Understanding **117**(10), 1468–1481 (2013)
11. Bergen, T., Wittenberg, T.: Stitching and surface reconstruction from endoscopic image sequences: A review of applications and methods. IEEE Journal of Biomedical and Health Informatics **20**(1), 304–321 (2016)
12. Bergen, T., Wittenberg, T., Münzenmayer, C., Chen, C.C.G., Hager, G.D.: A graph-based approach for local and global panorama imaging in cystoscopy. In: Proc. SPIE, Medical Imaging: Image-Guided Procedures, Robotic Interventions, and Modeling, vol. 8671. Lake Buena Vista, Florida, USA (2013)
13. Blender-Online-Community: Blender - a 3D modelling and rendering package (2014). URL `www.blender.org`
14. Carroll, R., Seitz, S.: Rectified surface mosaics. International Journal on Computer Vision **85**(3), 307–315 (2009)
15. Chan, M., Lin, W., Zhou, C., Qu, J.Y.: Miniaturized three-dimensional endoscopic imaging system based on active stereovision. Applied Optics **42**(10), 1888–1898 (2003)
16. Daul, C., Rösch, R., Claus, B.: Building a color classification system for textured and hue homogeneous surfaces: system calibration and algorithm. Machine Vision and Applications **12**(3), 137–148 (2000)
17. Hernández-Mier, Y., Blondel, W.C.P.M., Daul, C., Wolf, D., Guillemin, F.: Fast construction of panoramic images for cystoscopic exploration. Computerized Medical Imaging and Graphics **34**(7), 579–592 (2010)
18. Holzbeierlein, J., Lopez-Corona, E., Bochner, B., Herr, H., Donat, S., Russo, P., Dalbagni, G., Sogani, P.: Partial cystectomy: a contemporary review of the memorial Sloan-kettering cancer center experience and recommendations for patient selection. Journal of Urology **172**(3), 878–881 (2004)
19. Kaufman, A., Wang, J.: 3D surface reconstruction from endoscopic videos. In: L. Linsen, H. Hagen, B. Hamann (eds.) Visualization in Medicine and Life Sciences, Mathematics and Visualization, pp. 61–74. Springer Berlin Heidelberg (2008)
20. Kazhdan, M., Bolitho, M., Hoppe, H.: Poisson surface reconstruction. In: Fourth Eurographics symposium on Geometry processing, pp. 61–70. Cagliari, Italy (2006)
21. Miranda, R., Hernandez-Mier, Y., Daul, C., Blondel, W., Wolf, D.: Mosaicing of medical video-endoscopic images : data quality improvement and algorithm testing. In: International Conference on Electrical and Electronics Engineering (ICEEE) and Tenth Conference on Electrical Engineering (CIE). Acapulco Guerrero, Mexico (2004)
22. Miranda-Luna, R., Daul, C., Blondel, W., Hernández-Mier, Y., Wolf, D., Guillemin, F.: Mosaicing of bladder endoscopic image sequences: Distortion calibration and registration algorithm. IEEE Transactions on Biomedical Engineering **55**(2), 541–553 (2008)

23. Mountney, P., Yang, G.Z.: Dynamic view expansion for minimally invasive surgery using simultaneous localization and mapping. In: Int. Conf. of the IEEE Engineering in Medicine and Biology Society, pp. 1184–1187. Minneapolis, USA (2009)
24. Nelder, J.A., Mead, R.: A simplex method for function minimization. The computer journal **7**(4), 308–313 (1965)
25. Penne, J., Höller, K., Stürmer, M., Schrauder, T., Schneider, A., Engelbrecht, R., Feußner, H., Schmauss, B., Hornegger, J.: Time-of-flight 3-D endoscopy. Medical Image Computing and Computer-Assisted Intervention pp. 467–474 (2009)
26. Pluim, J., Maintz, J., Viergever, M.: Mutual-information-based registration of medical images: a survey. IEEE Trans. on Medical Imaging **22**(8), 986–1004 (2003)
27. Shevchenko, N., Fallert, J., Stepp, H., Sahli, H., Karl, A., Lueth, T.: A high resolution bladder wall map: Feasibility study. In: 34th Int. Conf. of the IEEE Engineering in Medicine and Biology Society, pp. 5761–5764. San Diego, CA (2012)
28. Soper, T., Porter, M., Seibel, E.J.: Surface mosaics of the bladder reconstructed from endoscopic video for automated surveillance. IEEE Transactions on Biomedical Engineering **59**(6), 1670–1680 (2012)
29. Weibel, T., Daul, C., Wolf, D., Rösch, R.: Contrast-enhancing seam detection and blending using graph cuts. In: 21st International Conference on Pattern Recognition, pp. 2732–2735. Tsukuba, Japan (2012)
30. Weibel, T., Daul, C., Wolf, D., Rösch, R., Guillemin, F.: Graph based construction of textured large field of view mosaics for bladder cancer diagnosis. Pattern Recognition **45**(12), 4138–4150 (2012)
31. Wu, C., Narasimhan, S., Jaramaz, B.: A multi-image shape-from-shading framework for near-lighting perspective endoscopes. International Journal of Computer Vision **86**(2-3), 211–228 (2010)
32. Wu, C.H., Sun, Y.N., Chang, C.C.: Three-dimensional modeling from endoscopic video using geometric constraints via feature positioning. IEEE Transactions on Biomedical Engineering **54**(7), 1199–1211 (2007)